

Continuous sterane and phytane $\delta^{13}\text{C}$ record reveals a substantial $p\text{CO}_2$ decline since the mid-Miocene

Received: 7 February 2022

Accepted: 8 April 2024

Published online: 18 June 2024

 Check for updates

Caitlyn R. Witkowski^{1,2}✉, Anna S. von der Heydt³, Paul J. Valdes⁴,
Marcel T. J. van der Meer¹, Stefan Schouten^{1,5} & Jaap S. Sinninghe Damsté^{1,5}

Constraining the relationship between temperature and atmospheric concentrations of carbon dioxide ($p\text{CO}_2$) is essential to model near-future climate. Here, we reconstruct $p\text{CO}_2$ values over the past 15 million years (Myr), providing a series of analogues for possible near-future temperatures and $p\text{CO}_2$, from a single continuous site (DSDP Site 467, California coast). We reconstruct $p\text{CO}_2$ values using sterane and phytane, compounds that many phytoplankton produce and then become fossilised in sediment. From 15.0–0.3 Myr ago, our reconstructed $p\text{CO}_2$ values steadily decline from 650 ± 150 to 280 ± 75 ppmv, mirroring global temperature decline. Using our new range of $p\text{CO}_2$ values, we calculate average Earth system sensitivity and equilibrium climate sensitivity, resulting in 13.9°C and 7.2°C per doubling of $p\text{CO}_2$, respectively. These values are significantly higher than IPCC global warming estimations, consistent or higher than some recent state-of-the-art climate models, and consistent with other proxy-based estimates.

Defining the relationship between the atmospheric concentration of carbon dioxide ($p\text{CO}_2$) and temperature is essential for understanding present environmental changes and modelling future climate trends. Geologic data can provide critical context, as well as possible analogues, for our future. For example, as compared to today's global annual temperatures of 14.5°C ¹, the middle Miocene (ca. 15 million years ago; Ma) was 18.4°C ^{2–4}, equivalent to that predicted for the year 2100 using the IPCC RCP8.5 scenario^{5,6}. Thus, studying the past 15 million years (Myr) may provide a series of climate analogues relevant for possible near-future climates.

Over the past 15 million years, $p\text{CO}_2$ values have steadily declined, according to the latest $p\text{CO}_2$ compilation⁷. Within this revised compilation, however, estimates widely range both among proxies and within a single proxy (i.e., >500 ppmv difference) and include some unrealistically low values (i.e., <120 ppmv), providing the need for additional independent proxy records. Furthermore, our current understanding of the past 15 Myr is comprised of compilations^{7–10} of

much shorter intervals, e.g., the recent study by Brown et al.¹¹ covering 5–7 Ma; no single site covers the entirety of the past 15 Myr, which introduces concerns in stitching disparate sections together (e.g., regional and latitudinal influences). Thus, $p\text{CO}_2$ reconstructions over the past 15 Myr require further clarification from an additional independent proxy record from a single site that spans this whole period, especially given the importance of defining the relationship between $p\text{CO}_2$ and temperature for future climate scenarios.

Here, we aim to better define the relationship between $p\text{CO}_2$ and temperature from the mid Miocene to late Pleistocene by using a single site that covers this entire 15-Myr time interval, supplemented with additional sites that cover shorter timespans within the same time interval. We use a refreshed approach to estimate $p\text{CO}_2$ from the stable carbon isotopic fractionation that occurs during photosynthetic CO_2 -fixation (ϵ_p). This isotopic fractionation occurs in photoautotrophs as their CO_2 -fixing enzyme Rubisco selects ^{12}C over ^{13}C , resulting in isotopically more negative biomass than the dissolved inorganic carbon

¹Department of Marine Microbiology and Biogeochemistry, NIOZ Royal Netherlands Institute for Sea Research, Den Burg (Texel) 1790AB, The Netherlands.

²Schools of Earth Science and Chemistry, and the Cabot Institute, University of Bristol, Bristol BS8 1RJ, UK. ³Institute for Marine and Atmospheric Research Utrecht, Department of Physics, Utrecht University, Utrecht 3584CC, The Netherlands. ⁴School of Geographical Sciences and Cabot Institute, University of Bristol, Bristol BS8 1SS, UK. ⁵Department of Geosciences, Utrecht University, Utrecht 3508 TA, The Netherlands. ✉ e-mail: caitlyn.witkowski@bristol.ac.uk

source (e.g., growth water). The ϵ_p framework assumes passive diffusion of $\text{CO}_{2[\text{aq}]}$ into photoautotroph cells and so the utilization of carbon-concentrating mechanisms by photoautotrophs in past oceans is an unavoidable limitation. However, three decades of field observations and laboratory cultures (e.g.^{12–20}) have attributed ambient $p\text{CO}_2$ as the primary controlling factor for ϵ_p , in which higher $p\text{CO}_2$ results in higher ϵ_p values. ϵ_p can be calculated from the $\delta^{13}\text{C}$ of phytoplanktonic biomass corrected for the $\delta^{13}\text{C}$ of dissolved CO_2 ($\text{CO}_{2[\text{aq}]}$). ϵ_p is then used to estimate the concentration of $\text{CO}_{2[\text{aq}]}$ via $\text{CO}_{2[\text{aq}]} = b / (\epsilon_f - \epsilon_p)$, where ϵ_f is the maximum potential fractionation due to CO_2 -fixation and b represents carbon demand per supply for phytoplankton. Finally, $\text{CO}_{2[\text{aq}]}$ is converted to atmospheric $p\text{CO}_2$ via Henry's law assuming atmosphere-ocean equilibrium. This b parameter represents physiological factors that may impact CO_2 uptake, e.g., growth rate, cell radius, and cell membrane permeability e.g.^{21,22}. Recent culture experiments suggest that light energy, independent of its effect on growth rate, may also be an important control, with higher irradiance resulting in higher ϵ_p values^{15,19,23,24}, but has not yet resulted in revisions to the $p\text{CO}_2$ proxy calculation. This recent work provides new and exciting questions to explore, making the application of ϵ_p for reconstructing $p\text{CO}_2$ in different settings and time periods timely, especially in context of the latest $p\text{CO}_2$ compilation⁷. By using a diversity of independent proxy methodologies, ideally with consistent deployment of methods between groups, with honest and robust modelling of uncertainty within each system, we can then challenge and scrutinize persistent proxy outliers that range outside the uncertainty bands of multiple other proxies.

Whereas previous work has relied on the $\delta^{13}\text{C}$ of alkenones i.e., compounds produced by species within the Haptophyte clade, we expand the ϵ_p approach to the $\delta^{13}\text{C}$ of general phytoplankton biomarkers (GPBs) i.e., compounds produced by the majority of photoautotrophs in sea surface waters and have subsequently become fossilized in marine sediments^{25,26}. Several recent studies explored the potential of GPBs across a modern environmental transect from high $p\text{CO}_2$ near a naturally-occurring marine CO_2 seep towards control values in two drastically different geographic locations (i.e., off the coasts of Vulcano Island, Italy²⁵ and Shikine Island, Japan²⁶). The applied GPBs known as phytol (i.e., the side-chain of the vital photoautotrophic pigment chlorophyll-*a*)²⁷ and cholesterol (i.e., a sterol that all eukaryotes synthesize or produce from ingested sterols with minimal isotopic fractionation^{28,29}) demonstrate that mixed phytoplankton communities with varying cell sizes and growth rates still exhibit a strong isotopic response to $\text{CO}_{2[\text{aq}]}$. Phytol has further been tested across glacial-interglacial cycles, which suggest phytol reconstructions were within error of the ice core-based CO_2 records and showed nearly identical values as the alkenone-based reconstructions³⁰. Phytol and sterols have less well-constrained sources than alkenones, possibly leading to more uncertainty in absolute $p\text{CO}_2$ estimates. However, because GPBs are produced by a large number of species, they may have several benefits over alkenones: (i) GPBs have greater spatial and temporal distribution (spanning at least 10x deeper in the geologic record)³¹ and (ii) GPBs have the potential to curb species-specific concerns and environmental effects by averaging the whole phytoplankton community, while also being much more specific than the $\delta^{13}\text{C}$ of bulk sedimentary OM that has been used to this end³². Because GPBs are far more ubiquitous than alkenones, they provide more extensive coverage (both spatially and temporally) to generate a continuous record of $p\text{CO}_2$, overcoming a major hurdle with previous proxy-based $p\text{CO}_2$ reconstructions. As such, GPBs have the potential to span the Phanerozoic, whereas alkenones are limited to the Cenozoic, which would extend ϵ_p -based $p\text{CO}_2$ proxies by nearly ten-fold. Thus, this general phytoplankton biomarker approach is a promising tool to obtain paleo $p\text{CO}_2$ records.

Here, we estimate paleo $p\text{CO}_2$ from the $\delta^{13}\text{C}$ of GPBs over the past 15 Myr, as well as from the $\delta^{13}\text{C}$ of alkenones for proxy comparison.

Results and discussion

$\delta^{13}\text{C}$ values of GPBs over the past 15 Myr at DSDP Site 467

Marine sediments retrieved by drilling DSDP Site 467 (33.8495, -120.757833) off the coast of California are remarkably unique in that they contain OM-rich sediments over this entire timeframe (details in “Methods”). The most abundant and ubiquitous GPBs in these sediments are phytane, 5α -cholestane, 24-ethyl- 5α -cholestane, and 24-methyl- 5α -cholestane, the diagenetic products of our target GPBs (i.e., phytol and sterols). These GPBs occurred in organic sulphur (S)-rich macromolecules and were recovered by desulfurization. Because reduced inorganic S species rapidly react with functionalized labile lipids in anoxic surface sediments, S-bound molecules reflect in situ produced lipids. The low abundance of higher plant-derived long-chain *n*-alkanes and terpenoids from terrestrial inputs indicate that sedimentary OM at Site 467 is predominantly derived from marine sources. Thus, these phytane and steranes originate primarily from phytoplankton that are photosynthetically fixing dissolved CO_2 in the upper part of the water column³³. Details on methods in Methods.

The $\delta^{13}\text{C}$ values of the GPBs steadily increase from 15.0 to 0.3 Ma (Fig. 1a; Supplementary Fig. 1; Supplementary Dataset 1–6). Here, we use a weighted average for the $\delta^{13}\text{C}$ of steranes, based on their fractional abundances (Supplementary Dataset 3–6). The $\delta^{13}\text{C}$ of phytane (ranging from -26.8 to -23.7‰) and weighted steranes (from -28.2 to -24.3‰) show statistically similar $\delta^{13}\text{C}$ trends throughout the record (Fig. 1, S3, S4), consistent with a similar general source, i.e., phytoplankton. These $\delta^{13}\text{C}$ records are consistent with the much shorter $\delta^{13}\text{C}$ records for GPBs (Supplementary Data 2) reported for the Monterey Formation at Naples Beach in the Santa Barbara basin³³ and Shell Beach in the Pismo basin³⁴, as well as for the $\delta^{13}\text{C}$ of phytane record from

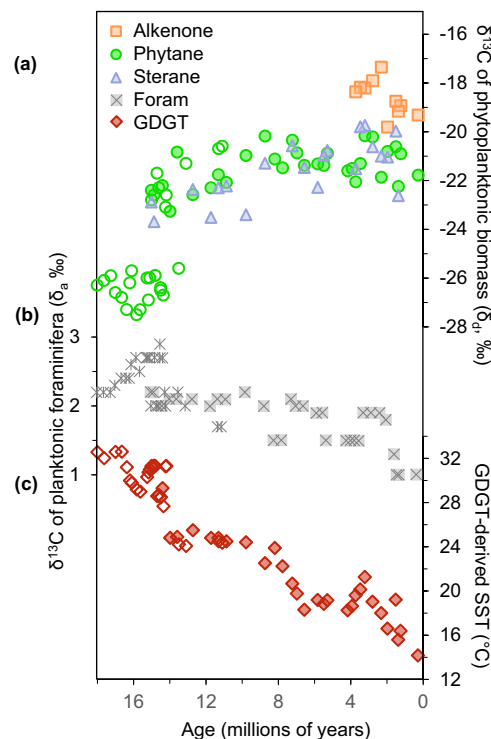


Fig. 1 | Data covering the past 18 Myr used to calculate the atmospheric concentration of carbon dioxide ($p\text{CO}_2$) from phytoplankton biomarkers. a $\delta^{13}\text{C}$ records of phytane (green circles), $\text{C}_{37:2}$ and $\text{C}_{37:3}$ alkenones (peach squares), and the weighted average of steranes (lavender triangle), **(b)** global compilation of $\delta^{13}\text{C}$ of planktonic foraminiferal shells³⁷, and **(c)** glycerol dibiphytanyl glycerol tetraethers (GDGTs)-derived sea surface temperatures (SSTs). For **(a)**, **(b)**, and **(c)**, the closed symbols refer to the values for Site 467 and open symbols refer to additional sites. Source data are provided with this paper (Supplementary Data 1–9).

DSDP Site 608 in King's Trough in the eastern North Atlantic^{3,35}. Although these three latter sections only span ca. 11–18 Ma, their corresponding results strongly suggest that the $\delta^{13}\text{C}$ records at DSDP Site 467 reflect a global (and not local) signal for $p\text{CO}_2$. Alkenones were present in only the most recent 4 Myr and their $\delta^{13}\text{C}$ values range from -21.4 to -23.8‰ (Fig. 1a; Supplementary Data 7), consistent with the $\delta^{13}\text{C}$ trends for the GPBs during that time.

Calculations for ε_p based on $\delta^{13}\text{C}$ values of GPBs

ε_p is calculated from the $\delta^{13}\text{C}$ of phytoplanktonic biomass (δ_p) and the $\delta^{13}\text{C}$ of aqueous carbon dioxide ($\text{CO}_{2[\text{aq}]}$) in the photic zone (δ_d):

$$\varepsilon_p = 1000 \cdot [(\delta_d + 1000) / (\delta_p + 1000) - 1] \quad (1)$$

To determine δ_p , we use the $\delta^{13}\text{C}$ of a phytoplanktonic biomarker lipid (Supplementary Fig. 1) corrected for the isotopic offset between the specific biomarker lipid and biomass (Fig. 1a). This offset is calculated based on compiled laboratory cultures, with the isotopic offset between biomass from phytane as $3.5 \pm 1.3 \text{ SD } \text{‰}$ based on its precursor phytol (compiled in ref. 36), steranes as $4.5 \pm 3.0 \text{ SD } \text{‰}$ based on their precursor sterols³⁷, and alkenones as $3.9 \pm 0.4 \text{ SD } \text{‰}$ (compiled in ref. 36). δ_d was estimated from a global compilation of $\delta^{13}\text{C}$ of planktonic foraminiferal shells³⁸ (Fig. 1b) and was corrected for the temperature-dependent carbon isotopic fractionation of $\text{CO}_{2[\text{aq}]}$ with respect to HCO_3^- ref. 39. Sea surface temperatures (SST) were calculated using the TEX_{86} proxy^{40,41} based on the ratio of cyclopentane rings in glycerol dibiphytanyl glycerol tetraethers (GDGTs) in the same sediments as our GPBs (Fig. 1c; Supplementary Data S8) and assigned an uncertainty of $\pm 4 \text{ }^\circ\text{C SD}^{40}$ caused by potential calibration errors. The estimated values for ε_p are compiled in Supplementary Fig. 2.

$p\text{CO}_2$ was then calculated using^{22,42}:

$$p\text{CO}_2 = [b / (\varepsilon_f - \varepsilon_p)] / K_0 \quad (2)$$

where K_0 reflects the Henry's Law constant that is used to convert $\text{CO}_{2[\text{aq}]}$ to $p\text{CO}_2$ based on temperature and salinity⁴³. Within the brackets of Eq. (2), ε_f reflects the maximum potential isotopic fractionation due to CO_2 -fixation by the enzyme Rubisco⁴⁴, which is $26.5 \pm 1.5 \text{ ‰}$ uniformly distributed uncertainty to reflect the full potential range reported in algal cultures (compiled in ref. 36). The b parameter reflects species carbon demand per supply^{22,42}, which was back-calculated from bulk OM and phytol in a compilation of modern surface sediments worldwide³⁶ (i.e., 28 sites at different latitudes with known environmental parameters): the average is $168 \pm 43 \text{ SD } \text{‰ kg } \mu\text{M}^{-1}$. This value for b is further supported by two phytol studies across two naturally occurring steep CO_2 gradients^{25,26} and a phytol study in the equatorial Pacific Ocean⁴⁵, as well as previous paleoclimate studies using phytane where a b value of $170 \text{ ‰ kg } \mu\text{M}^{-1}$ was used^{46–48}. Thus, we apply $168 \text{ ‰ kg } \mu\text{M}^{-1}$ in all our calculations.

$p\text{CO}_2$ estimations over the past 15 Ma

Expectedly, ε_p calculated from the $\delta^{13}\text{C}$ of GPBs also all share similar values, ranges, and declining trends: 15.8 to 11.2 ‰ for phytane and 17.0 to 11.0 ‰ for steranes (Supplementary Fig. 2; Supplementary Dataset 1–6). This similarity among the GPBs is likewise reflected in the resulting $p\text{CO}_2$ estimations (Fig. 2). $p\text{CO}_2$ is highest at 15.0 Ma with values of 620 ppmv and 655 ppmv using phytane and steranes, respectively. These estimates tightly follow each other throughout the record, with the exception of the data point at 9.8 Ma , where phytane suggests a continued decline (435 ppmv) but steranes suggests a singular spike in $p\text{CO}_2$ (540 ppmv). By 8.7 Ma , phytane and sterane estimates converge (400 ppmv) for the rest of the record. Alkenone-based $p\text{CO}_2$ estimations, which could only be determined for the most recent 4 Myr period, where alkenones were present, were almost identical to those obtained with the GPBs.

The similarity in $p\text{CO}_2$ estimations between these GPBs is reassuring. However, we consider that these estimations may be influenced by the same factors, such as constraints on calculation parameters or upwelling. One of the more-difficult-to-constrain parameters in our calculation is factor b . Although it may change over time²¹, it is not possible to constrain this value in most geologic settings; thus, maintaining b as a constant is the most reasonable approach. Sensitivity tests demonstrate that the uncertainty within the b value could lead up to a maximum of 25% change in $p\text{CO}_2$ estimation³⁶, which is still too small to account for the consistent decline over the studied time interval. Furthermore, the overlap between our GPB-based $p\text{CO}_2$ estimates with the more conventional alkenone-based $p\text{CO}_2$ estimates, for which substantial research on the b -value has been conducted^{20,42}, suggests that b values for our GPB-based reconstructions are realistic.

Another potential factor to consider is change in upwelling intensity. Upwelling may mask the phytoplankton response to a changing $p\text{CO}_2$, bringing the ocean out of equilibrium with the atmosphere as upwelling brings more ^{13}C -depleted $\text{CO}_{2[\text{aq}]}$ from cold bottom waters to the surface⁴⁵. Radiolarian evidence⁴⁹ at the nearby ODP Site 1021 suggests enhanced coastal upwelling is unlikely in this region due to the timing of biosiliceous sedimentation in relation to known changes in the California Current. A potential increased production of North Atlantic Deep Water (NADW), the source of upwelling in this region, may have occurred between 11.5 to 10.0 Ma and from 7.6 to 6.5 Ma ⁴⁹ (marked in Fig. 2). Notably, during these potential periods of increased NADW (Fig. 2), our biomarker-based $p\text{CO}_2$ values do not deviate from the overall downward trend. To further explore the potential impact of upwelling from a biomarker-perspective, we also analyzed the C_{25} highly branched isoprenoids (HBI), a biomarker produced by specific diatoms that thrive in upwelling regions, as seen in the Arabian Sea over the past 0.3 Myr ⁵⁰. Although the diatom-produced C_{25} HBI is present in our sediments, the $\delta^{13}\text{C}$ of the C_{25} HBI varies greatly throughout the record and has no correlation with the $\delta^{13}\text{C}$ of the GPBs (Supplementary Fig. 1, 3). This lack of correlation suggests that these upwelling-related diatom species do not significantly contribute to the overall phytoplankton lipid pool and thus the effect of upwelling is likely minimal. We also considered the relative contribution of the C_{28} sterane (24-methyl-5 α -cholestane), which tends to be more dominant in diatoms; however, again, there is no relationship between the fractionation abundance of these diatom produced biomarkers with these periods of potential upwelling. Overall, although productivity changes or upwelling could play some role, these factors alone cannot account for our reconstructed ca. 350 ppmv decline in $p\text{CO}_2$ over 15 Myr .

Here, we put our results into context of earlier reports. We find that as compared with^{19,51,52} the recently revised alkenone- and boron-based $p\text{CO}_2$ proxies compiled in Rae et al.⁷ (Fig. 3a), our $p\text{CO}_2$ estimations follow similar trends and fall within error of estimate in Rae et al.⁷, with absolute values closely matching throughout the record, especially the boron-based $p\text{CO}_2$ estimations. In the most recent 4 Myr of our record where our sediments contained alkenones, our $p\text{CO}_2$ values closely match the boron-based $p\text{CO}_2$ in Rae et al.⁷, but tend to be slightly higher (ca. 50 ppmv) than the⁷ alkenone-based $p\text{CO}_2$ estimations in Rae et al.⁷. This overall alignment with the most up-to-date records is promising; this suggests that our GPB-based values are likely producing reasonable $p\text{CO}_2$ estimations, but in this case, from a single continuous proxy record.

Furthermore, it is notable that our GPB-based $p\text{CO}_2$ estimates are consistent with the $p\text{CO}_2$ required by the majority of climate models in order to agree with the proxy-derived temperature estimates (and the generally accepted sensitivity to $p\text{CO}_2$). For the mid-Miocene Climate Optimum (17–15 Ma), two different versions of the National Centre for Atmospheric Research model (NCAR) indicate that $p\text{CO}_2$ needs to be within the range 460 – 580 ppmv ^{2,51}, the Max-Planck Institute Earth System Model (MPI-ESM) suggests that $p\text{CO}_2$ should be around

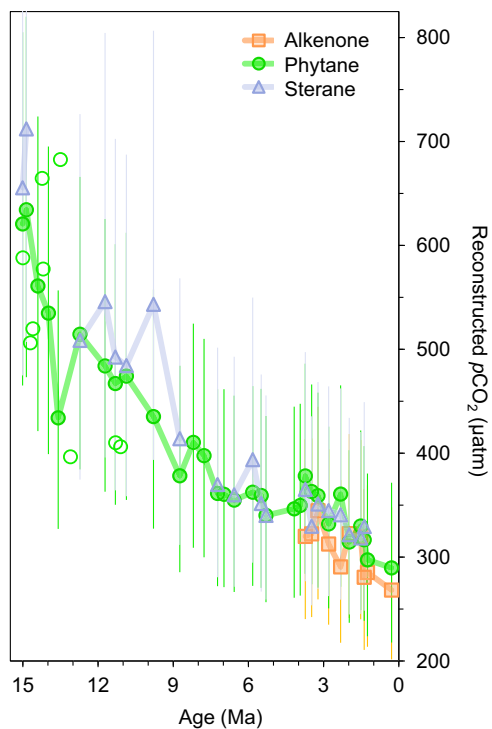


Fig. 2 | Estimates for atmospheric concentration of carbon dioxide ($p\text{CO}_2$) derived from DSDP Site 467. Covering the past 15 million years, $p\text{CO}_2$ calculations are based on the $\delta^{13}\text{C}$ records of phytane (green circles), $\text{C}_{37:2}$ and $\text{C}_{37:3}$ alkenones (peach squares), and the weighted average of steranes (lavender triangle). Closed symbols represent Site 467, open symbols refer to additional sites. Error bars represent the one standard deviation based on Monte Carlo simulations that compound uncertainties for all input parameters. Shaded areas show two points of potentially-enhanced North Atlantic Deep Water. Source data are provided with this paper (Supplementary Data 1–9).

720 ppmv⁵², and Community Earth System Model (CESM1.0) requires around 800 ppmv⁵¹. Knorr et al.⁵³ did succeed in simulating the warmth of the mid-Miocene Climatic Optimum with relatively low $p\text{CO}_2$ but only by adopting large changes to the vegetation distribution, reducing planetary albedo, and having a strong positive water vapour feedback in their climate model. Therefore, our $p\text{CO}_2$ estimates are aligned with model-based interpretations of what reasonable $p\text{CO}_2$ should be across this period.

We also considered how our GPB-based $p\text{CO}_2$ estimations relate to proxy-based temperature. Based on visual comparison over this period (Fig. 3), it is clear that our $p\text{CO}_2$ record shows a similar declining trend as two different temperature proxies (Fig. 3b): the alkenone derived U^{K}_{37} proxy¹⁰, which represents SST, and the $\delta^{18}\text{O}$ derived from benthic foraminifera⁵⁴, which represents oceanic bottom water temperature, as well as the build-up of the continental ice volume. The remarkably similar trends of our $p\text{CO}_2$ estimates and independent temperature records from the Miocene through to the Pliocene therefore suggest that $p\text{CO}_2$ and temperature are closely coupled. A potential caveat for this observed correlation is the fact that SST is used twice in our paleo $p\text{CO}_2$ estimation (although notably, we have used the SST proxy TEX_{86} to calculate our $p\text{CO}_2$, whereas our temperature comparisons in Fig. 3b are derived from different temperature proxies). Sensitivity tests over the Phanerozoic show negligible effects of SST on the first use in the equations, when calculating ϵ_p ($\pm 0.5\%$). In the second use of SST in the calculations (converting $\text{CO}_{2[\text{aq}]}$ to $p\text{CO}_2$), sensitivity tests show that SST may potentially affect $p\text{CO}_2$ estimations up to ± 50 ppmv³⁶. Although a sizeable error, this potential ± 50 ppmv is too small to suggest SST alone is driving the

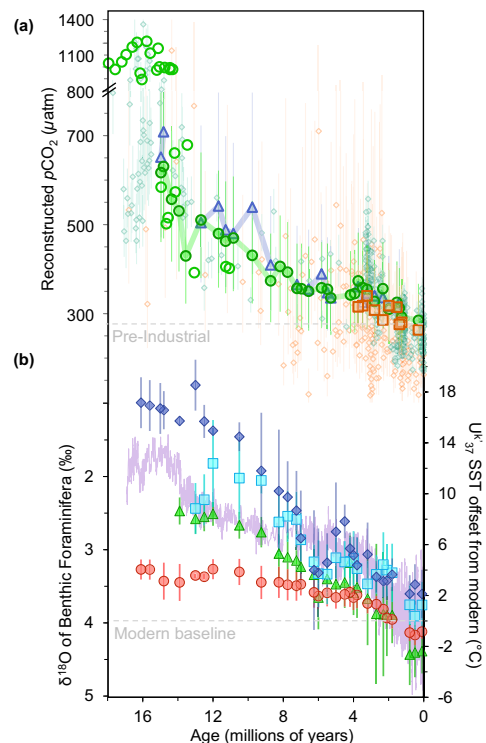


Fig. 3 | Reconstructed the atmospheric concentration of carbon dioxide ($p\text{CO}_2$) and temperature estimates over the past 18 Ma. **a** $p\text{CO}_2$ estimations based on the $\delta^{13}\text{C}$ records of phytane (green circle, with closed symbols for Site DSDP 467, open symbols for additional sites), alkenones (peach squares), and the weighted average of steranes (lavender triangle). Error bars represent the one standard deviation based on Monte Carlo simulations that compound uncertainties for all input parameters. Previously compiled $p\text{CO}_2$ estimations⁷ in diamond, alkenones (peach) and boron (teal). **b** Changes in U^{K}_{37} -based mean annual sea surface temperature (SST) relative to modern¹⁰ high-latitudes for the Northern Hemisphere (NH, blue), mid-latitudes (30–50°) for the NH (cyan) and Southern Hemisphere (SH, green), and tropics (30°N–30°S, red). Compiled $\delta^{18}\text{O}$ derived from benthic foraminifera⁵⁴ (lavender) indicate bottom water temperature and build-up of continental ice volume. Source data are provided with this paper (Supplementary Data 1–9) or references therein.

declining trend ranging from ca. 630 to 280 ppmv over the entire record.

Climate sensitivity

To explore the precise relationship between $p\text{CO}_2$ and global temperature, we calculated climate sensitivity, which refers to the impact of radiative forcing (which is primarily impacted by $p\text{CO}_2$) on temperature. Here, we calculate both Earth system sensitivity (ESS) and equilibrium climate sensitivity (ECS), respectively representing slow and fast climate feedback responses, using our new $p\text{CO}_2$ dataset from DSDP 467 (Table 1). We calculate an average sensitivity over 15 Myr and a range of $p\text{CO}_2$ values. Any variations over time could come from subsets of these points but given that there are a limited number (i.e., 30) of different (unequally spaced) time values, subdivisions and new regressions with all uncertainties would most likely give non-significant fits. The temporal dependence of climate sensitivity can only be determined with higher temporal resolution records for specific time intervals.

First, we calculate ESS, i.e., the response to CO_2 including (slow) climate feedbacks. ESS was estimated for each latitudinal region using a linear regression between the change in mean annual SST relative to modern SST (ΔSST) and radiative forcing due to CO_2 ($\Delta\text{R}_{\text{CO}_2}$ [Wm^{-2}]).

Table 1 | Sensitivity of temperature to carbon dioxide (CO₂)

Region	Equilibrium Climate Sensitivity (ECS)			Earth System Sensitivity (ESS)		
	K / Wm ⁻²	r ²	°C / 2×CO ₂	K / Wm ⁻²	r ²	°C / 2×CO ₂
NH High Latitude	3.1	0.9	11.6	5.1	0.8	18.8
NH Mid Latitude	2.3	0.9	8.6	4.3	0.8	16.0
SH Mid Latitude	2.2	0.8	8.3	4.4	0.6	16.1
Tropics ^a	1.3	0.8	5.0	3.0	0.5	11.1
Global	1.9	0.8	7.2	3.8	0.6	13.9

^aU^K₃₇ ratio at these sites is reaching saturation (i.e., 1.00) from 15 to 8 Ma and SSTs derived from these reconstructed SSTs were omitted in our calculation.

Estimated Equilibrium Climate Sensitivity (ECS, fast feedbacks) and Earth System Sensitivity (ESS, slow feedbacks) over 15.0–0.3 Ma. ECS and ESS are expressed in temperature per radiative forcing (K/Wm⁻²), the units typically used²⁴ for S_[CO₂,X,Y], and temperature change per doubling in CO₂ (°C/2×CO₂) based on their linear fit with errors in x and y. Calculations are shown by latitudinal region, including northern hemisphere (NH) and southern hemisphere (SH). Global refers to the weight by percent-area for the Earth: tropics (30°N–30°S, 50.0%), mid-latitudes (30–60°, 36.6%), and high latitudes (60–90°, 13.4%).

ΔSST is based on the U^K₃₇ proxy for SST, which were compiled¹⁰ by latitude and hemisphere into 0.125 Ma bins (Fig. 3b) and linearly interpolated for the age of our sediments (Fig. 4). Tropical SSTs may be underestimated from 15 to 8 Ma, given that the U^K₃₇ ratio is approaching saturation at these sites, and so to maintain consistency in proxy method but avoid bias in the tropic SSTs, we have not included U^K₃₇ values when it approaches 1.0 in our calculations. ΔR_{CO₂} was calculated using only the phytane-based pCO₂ record of DSDP 467, given that the GPBs and alkenones show similar pCO₂ values throughout this record and because the phytane record is most complete. Furthermore, phytane has yielded secular trends in pCO₂ comparable to other proxies in the Cretaceous^{31,48} and over the Phanerozoic³⁶. Monte Carlo simulations were used to propagate uncertainty for each equation parameter in these calculations³⁶.

The resulting ESS shows 18.8 °C (per CO₂-doubling) for NH high latitudes, 16.0 °C for the mid-latitudes, and 11.1 °C for the tropics (Supplementary Fig. 5), with respective values in K/Wm⁻² shown in Table 1 and are based on the slope of a linear fit of the data. When we weigh each sensitivity by the percent-area for the Earth: tropics (30°N–30°S, 50.0%), mid-latitudes (30–60°, 36.6%), and high latitudes (60–90°, 13.4%), our global average ESS amounts to 13.9 °C per doubling of CO₂. These values are considerably higher than the global ESS of 2.2 to 5.6 °C per CO₂-doubling calculated for the Plio-Pleistocene⁵⁵, although ESS from the same data (taking into account individual shifts in time) has been estimated as 9.0 ± 2.7 °C per CO₂-doubling (68% confidence level)^{56,57} which is more consistent with our values, even though we use a similar approach (long-time average) as ref. 55. Our mid- and high-latitude ESS estimates suggest significant polar amplification despite generally less-than-present ice cover. Recent modeling efforts have highlighted the importance of cloud feedbacks in explaining very high polar sensitivity^{58,59}. Even in largely ice-free climates of the Cenozoic, models suggest strong polar amplification due to cloud and land-surface feedbacks^{60,61}. That said, the Cenozoic CO₂PIP⁷ estimations for ESS exceed ca. 8 °C per CO₂-doubling for the past 20 Myr, reaching ca. 13 °C per CO₂-doubling in the early Cenozoic.

Next, we calculate ECS, i.e., fast climate feedback and the quantity generally used in policy discussions. Given that our record spans 15.0 to 0.3 Ma, during which there is large variability in ice sheet coverage, we additionally consider radiative forcing due to land ice change (ΔR_{LI}) based on earlier work^{55,62,63}, with results shown in Fig. 4. ECS was determined by a linear regression of ΔSST versus ΔR_{CO₂+LI} and is estimated to be 11.6 °C (per CO₂ doubling) for NH high latitudes, 8.6 °C for the mid-latitudes, and 5.0 °C for the

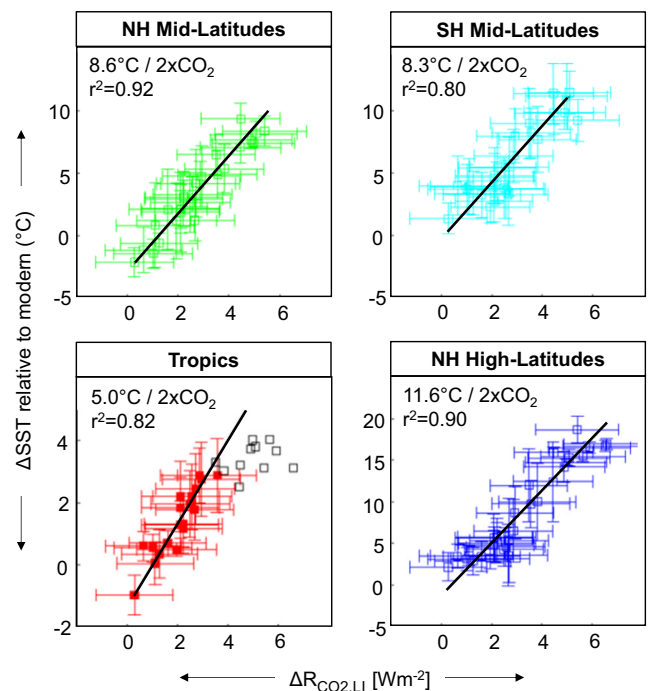


Fig. 4 | Relationship between radiative forcing due to carbon dioxide (CO₂) and temperature from 15.0–0.3 Ma. Y-axis: U^K₃₇-based sea surface temperature (SST) changes relative to the modern mean annual SST at each site¹⁰: northern hemisphere (NH) mid-latitudes (green), southern hemisphere (SH) mid-latitudes (cyan), tropics (red), and NH high latitudes (blue). Error bars represent the one standard deviation based on Monte Carlo simulations that compound uncertainties for all input parameters. *Note that the U^K₃₇ ratio approaching saturation beyond 8 Ma in the tropics cannot be used for a good computation of climate sensitivity, thus data > 8 million years (open black squares) are plotted but removed from fit. X-axis: Radiative forcing due to CO₂ and land-ice (ΔR_{CO₂,LI}), where CO₂ estimations are derived from the general phytoplankton biomarker phytane. Top left corners show equilibrium climate sensitivity change in temperature per doubling of CO₂ based on the slope of a linear fit of the proxy-based data. Source data are provided with this paper (Supplementary Data 2) and references therein.

tropics, with respective values in K/Wm⁻² and r² values shown in Table 1. When we again weigh each sensitivity by the percent-area for the Earth, our global average ECS is 7.2 °C per doubling of CO₂, much higher than the most recent IPCC estimates of 2.3 to 4.5 °C⁶ and consistent with some of the latest state-of-the-art models which suggest ca. 5.2 °C⁶⁴. It should be noted that our ECS is not the same as the ECS used by the IPCC, given that it represents specific climate sensitivity S_[CO₂,LI] (i.e., ESS corrected for potential slow land ice feedback) and does not consider changes in other greenhouse gases (e.g., methane), paleogeography, nor solar luminosity; we are currently unable to conduct these additional considerations⁶⁵. The impact of additional methane and water would bring down ECS, which likely explains why paleo ECS is generally higher than modern models.

Our work represents the application of general phytoplankton biomarkers (GPB) to reconstruct pCO₂ values, offering a refreshed approach to the pCO₂ proxy based on photosynthetic isotopic fraction that may enable reconstructions over longer timescales where other existing proxies are lacking (e.g., the Phanerozoic). Our reconstructed pCO₂ values across the past 15 million years suggest Earth system sensitivity averages 13.9 °C per doubling of pCO₂ and equilibrium climate sensitivity averages 7.2 °C per doubling of pCO₂. Although these values are significantly higher than IPCC global warming estimations, they are consistent or higher than some recent state-of-the-art climate models and consistent with other proxy-based estimates.

Methods

Study site

Site 467 (33.8495, -120.757833) was collected by Deep Sea Drilling Project Leg 63 at the San Miguel Gap off the coast of California, USA. The total length of the core section is 1041.5 m and 426.3 m were recovered. The core has the best-preserved organic matter of Leg 63⁶⁶, likely due to incorporation of abiotic sulphur species into labile functionalized lipids, a process which occurs rapidly during very early diagenesis^{67–69}. The age model is based on diatom, coccolith, and radiolarian events⁶⁶, which we have revised for every reported species using first and last occurrence, checked against the most up-to-date period tie points⁵⁴, and reported alongside mbsf from the core (details and references within Supplementary Data 9). The present-day oceanic regime of this region comprises of the California Current, a part of the North Pacific subtropical gyre which carries cold, fresher surface water from the North Pacific into the warmer, more saline surface water of the subtropical regions. Over long timescales, orbital forces impact the latitudinal changes, strength, and mean transport of the California Current flow.

Analytical methodology

Thirty-five marine sediments, depths ranging from 9 to 1038 mbsf, were sampled approximately every 30 m from the Site 467 core (Dataset S1). 15–20 g of homogenized sediments were extracted on a Dionex 250 accelerated solvent extractor at 100 °C, 7.6×10^6 Pa, using dichloromethane (DCM):methanol (MeOH) (9:1 v/v) and the extracts were dried over Na₂SO₄. The extracts were eluted over an alumina packed column and separated into an apolar (hexane:DCM, 9:1 v/v), ketone (DCM), and a polar fraction (DCM:MeOH, 1:1 v/v). Polar fractions were desulfurized using Raney-nickel, eluted over an alumina packed column into an apolar fraction (hexane:DCM, 9:1 v/v) and hydrogenated using acetic acid and platinum oxide^{67,68}. These were left over night and then cleaned over a small column of magnesium sulphate and sodium carbonate with DCM. To obtain baseline separation of the targeted biomarkers, *n*-alkanes were removed using vacuum-oven prepared 5 Å molecular sieve added to the samples, dissolved in cyclohexane, and left overnight; the supernatant was then removed and analyzed.

An Agilent 7890 A gas chromatograph-mass spectrometer (GC-MS) was used to identify GPBs (i.e., phytane and steranes), and the C₂₅ HBI alkane in the resulting apolar fraction from the desulfurized polar fraction, as well as alkenones in the ketone fractions. An Agilent 7890B GC with flame ion detector (FID) was used to determine compound quantities prior to injection on a Thermo Trace 1310 GC coupled to a Thermo Delta V-isotope ratio mass spectrometer (IRMS). GC-MS, GC-FID, and GC-IRMS measurements were conducted on a CP-Sil 5 column (25 m × 0.32 mm; d_f 0.12 μm). GC-MS and GC-FID used constant pressure and IRMS used constant flow of He carrier gas. All three instruments used the same GC program with starting oven temperatures of 70 °C ramped at 20 °C/min to 130 °C and then ramped at 4 °C/min to 320 °C for 10 min. For IRMS measurements, a standard with *n*-alkanes (C₂₀ and C₂₄) with known isotopic values (−32.7 and −27.0‰, respectively) was run at the start of each day and then co-injected with samples to monitor the integrity of the instrument (within 0.5‰). At the start of each day, the IRMS underwent an oxidation sequence for 10 min, He backflushed after oxidation for 5 min, and conditioning line purged for 5 min; a shorter version of this sequence is conducted in a post-sample seed oxidation, which includes 2 min oxidation, 2 min He backflush, and 2 min purge conditioning line.

An Agilent 1260 ultra-high-performance liquid chromatography (UHPLC) coupled to a 6130 quadrupole MSD in selected ion monitoring mode was used to identify and integrate glycerol dibiphytanyl glycerol tetraethers (GDGTs) in the polar fraction. Separation was achieved on two UHPLC silica columns (BEH HILIC columns, 2.1 × 150 mm, 1.7 μm; Waters) in series, fitted with a 2.1 × 5 mm pre-column of the same material (Waters) and maintained at 30 °C

according to previously established methods^{69–71}. With these GDGTs, we then apply the SST proxy known as TEX₈₆ (TetraEther index of tetraethers consisting of 86 carbon atoms), where the number of cyclopentane moieties increases along with SST⁴⁰. Here, we use the modified version known as TEX₈₆-H, modified for (sub)tropical oceans and greenhouse periods where the function excludes crenarchaeol regio-isomer for (sub)polar oceans^{40,72,73}. Because several minor isoGDGT were below the detection level in the deepest part of the studied section, it was not possible to obtain TEX₈₆ values. To accommodate for this, we compared the overall records from Site 467 to the TEX₈₆ values at Site 608 at the same latitude, as well as U_K³⁷ values from the nearby Site 1010 (directly south of DSDP Site 467) and Site 1021 (directly north of DSDP 467); all four sites have near-identical SST values throughout the past 15 Myr, so we use these other sites to linearly extrapolate the several missing SSTs at Site 467. All raw data is available in Supplementary Data 8.

Estimating climate sensitivity

ESS was then estimated for each latitude region using a linear regression of radiative forcing due to CO₂ (ΔR_{CO2}) versus ΔSST. ΔR_{CO2} was calculated using:

$$\Delta R_{CO_2} = [a_1(C - C_0)^2 + b_1|C - C_0| + c_1N_0 + 5.36] \times \ln(C/C_0) \quad (3)$$

where *C* is *p*CO₂ at the time of forcing (our phytane-based *p*CO₂), *C*₀ is a reference *p*CO₂ (280 ppm), *N*₀ is the average concentration of N₂O, and the constant coefficients *a*₁, *b*₁, and *c*₁ are 2.4×10^{-7} , 7.2×10^4 , and $2.1 \times 10^{-4} \text{ Wm}^{-2} \text{ ppm}^{-1}$, respectively, based on previously established methods⁷². For ΔSST, we used the previously compiled¹⁰ U_K³⁷-based SSTs (expressed relative to the modern SST at each site) by latitude: northern hemisphere (NH) high-latitudes (Ocean Drilling Program Sites 883, 907, 982, 983), NH mid-latitudes (ODP Sites 1010, 1021, 1208), southern hemisphere (SH) mid-latitudes (ODP Sites 594, 1085, 1088, 1125), and tropics (ODP Sites 722, 846, 850, 1241, U1338) from the U_K³⁷-proxy.

Given that this record spans 15.0 to 0.3 Ma, during which the ice sheet cover varied to a large extent, we also consider radiative forcing due to land ice change (ΔR_{LI}) which we estimated by multiplying reconstructed sea level (m) by 0.0308 Wm^{-3} , based on earlier work^{64,74}. Sea level over the last 16 Ma is estimated at a few instances (0 Ma = 0 m change in sea level relative to present⁷² and 3.2 Ma = 24 m, 10.0 Ma = 67 m, 14.9 Ma = 66 m, and 19.5 Ma = 105 m)⁷³ and then linearly interpolated. ECS is then approximated by the specific climate sensitivity S_[CO2,LI] (nomenclature is in Palaeosens⁶²), which we determine by a linear regression of SST anomaly versus ΔR_{CO2} + ΔR_{LI}.

Data availability

All data are generated and used in this study are available in the main text and/or the Supplementary Data 1–9.

References

- Hansen, J., Ruedy, R., Sato, M. & Lo, K. Global surface temperature change. *Rev. Geophys.* <https://doi.org/10.1029/2010RG000345> (2010).
- You, Y., Huber, M., Müller, R. D., Poulsen, J. & Ribbe, J. Simulation of the Middle Miocene Climate Optimum. *Geophys. Res. Lett.* <https://doi.org/10.1029/2008GL036571> (2009).
- Super, J. R. et al. North Atlantic temperature and *p*CO₂ coupling in the early-middle Miocene. *Geology* <https://doi.org/10.1130/G40228.1> (2018).
- Shevenell, A. E., Kennett, J. P. & Lea, D. W. Middle Miocene Southern Ocean cooling and Antarctic cryosphere expansion. *Science* (1979) <https://doi.org/10.1126/science.1100061> (2004).
- Etmann, M., Myhre, G., Highwood, E. J. & Shine, K. P. Radiative forcing of carbon dioxide, methane, and nitrous oxide: A significant

- revision of the methane radiative forcing. *Geophys. Res. Lett.* <https://doi.org/10.1002/2016GL071930> (2016).
- Sherwood, S. C. et al. An assessment of earth's climate sensitivity using multiple lines of evidence. *Rev. Geophys.* **58**, e2019RG000678 (2020).
 - Consortium*, T. C. C. P. I. P. (CenCO2PIP). et al. Toward a Cenozoic history of atmospheric CO₂. *Science (1979)* **382**, eadi5177 (2023).
 - Rae, J. W. B. et al. Atmospheric CO₂ over the Past 66 Million Years from Marine Archives. *Annu Rev. Earth Planet Sci.* **49**, 609–641 (2021).
 - Foster, G. L., Royer, D. L. & Lunt, D. J. Future climate forcing potentially without precedent in the last 420 million years. *Nat. Commun* (2017) <https://doi.org/10.1038/ncomms14845>.
 - Herbert, T. D. et al. Late Miocene global cooling and the rise of modern ecosystems. *Nat. Geosci.* <https://doi.org/10.1038/ngeo2813> (2016).
 - Brown, R. M., Chalk, T. B., Crocker, A. J., Wilson, P. A. & Foster, G. L. Late Miocene cooling coupled to carbon dioxide with Pleistocene-like climate sensitivity. *Nat. Geosci.* **15**, 664–670 (2022).
 - Wolhowe, M. D., Prah, F. G., Langer, G., Oviedo, A. M. & Ziveri, P. Alkenone δD as an ecological indicator: A culture and field study of physiologically-controlled chemical and hydrogen-isotopic variation in C₃₇ alkenones. *Geochim Cosmochim. Acta* **162**, 166–182 (2015).
 - Fry, B. & Wainright, S. C. Diatom of source of ¹³C-rich carbon in marine food webs. *Mar. Ecol. Prog. Ser.* **76**, 149–157 (1991).
 - Rau, G. H., Takahashi, T., Des Marais, D. J., Repeta, D. J. & Martin, J. H. The relationship between δ¹³C of organic matter and [CO_{2(aq)}] in ocean surface water: Data from a JGOFS site in the northeast Atlantic Ocean and a model. *Geochim Cosmochim. Acta* **56**, 1413–1419 (1992).
 - Phelps, S. R., Stoll, H. M., Bolton, C. T., Beaufort, L. & Polissar, P. J. Controls on Alkenone Carbon Isotope Fractionation in the Modern Ocean. *Geochim., Geophys. Geosyst.* **22**, e2021GC009658 (2021).
 - Popp, B. N., Kenig, F., Wakeham, S. G., Laws, E. A. & Bidigare, R. R. Does growth rate affect ketone unsaturation and intracellular carbon isotopic variability in *Emiliana huxleyi*? *Paleoceanography* **13**, 35–41 (1998).
 - Francois, R. et al. Changes in the δ¹³C of surface water particulate organic matter across the subtropical convergence in the SW Indian Ocean. *Glob. Biogeochem. Cycles* **7**, 627–644 (1993).
 - Laws, E. A., Popp, B. N., Bidigare, R. R., Kennicutt, M. C. & Macko, S. A. Dependence of phytoplankton carbon isotopic composition on growth rate and [CO_{2(aq)}]: Theoretical considerations and experimental results. *Geochim Cosmochim. Acta* **59**, 1131–1138 (1995).
 - Stoll, H. M. et al. Upregulation of phytoplankton carbon concentrating mechanisms during low CO₂ glacial periods and implications for the phytoplankton pCO₂ proxy. *Quat. Sci. Rev.* **208**, 1–20 (2019).
 - Laws, E. A. et al. Controls on the molecular distribution and carbon isotopic composition of alkenones in certain haptophyte algae. *Geochim. Geophys. Geosyst.* <https://doi.org/10.1029/2000gc000057> (2001).
 - Zhang, Y. G., Henderiks, J. & Liu, X. Refining the alkenone-pCO₂ method II: Towards resolving the physiological parameter 'b'. *Geochim. Cosmochim. Acta* **281**, 118–134 (2020).
 - Rau, G. H., Riebesell, U. & Wolf-Gladrow, D. A model of photosynthetic ¹³C fractionation by marine phytoplankton based on diffusive molecular CO₂ uptake. *Mar. Ecol. Prog. Ser.* <https://doi.org/10.3354/meps133275> (1996).
 - Rost, B., Zondervan, I. & Riebesell, U. Light-dependent carbon isotope fractionation in the coccolithophorid *Emiliana huxleyi*. *Limnol. Oceanogr.* **47**, 120–128 (2002).
 - Wilkes, E. B., Carter, S. J. & Pearson, A. CO₂-dependent carbon isotope fractionation in the dinoflagellate *Alexandrium tamarense*. *Geochim. Cosmochim. Acta* **212**, 48–61 (2017).
 - Freeman, K. H. & Hayes, J. M. Fractionation of carbon isotopes by phytoplankton and estimates of ancient CO₂ levels. *Global Biogeochem. Cycles* <https://doi.org/10.1029/92GB00190> (1992).
 - Hayes, J. M., Strauss, H. & Kaufman, A. J. The abundance of ¹³C in marine organic matter and isotopic fractionation in the global biogeochemical cycle of carbon during the past 800 Ma. *Chem. Geol.* **161**, 103–125 (1999).
 - Witkowski, C. R., van der Meer, M. T. J., Smit, N. T., Sinninghe Damsté, J. S. & Schouten, S. Testing algal-based pCO₂ proxies at a modern CO₂ seep (Vulcano, Italy). *Sci. Rep.* **10**, 10508 (2020).
 - Witkowski, C. R. et al. Validation of carbon isotope fractionation in algal lipids as a pCO₂ proxy using a natural CO₂ seep (Shikine Island, Japan). *Biogeosciences* **16**, 4451–4461 (2019).
 - Kohnen, M. E. L., Sinninghe Damsté, J. S., Baas, M., Dalen, A. C. K. V. & de Leeuw, J. W. Sulphur-bound steroid and phytane carbon skeletons in geomacromolecules: Implications for the mechanism of incorporation of sulphur into organic matter. *Geochim Cosmochim. Acta* [https://doi.org/10.1016/0016-7037\(93\)90414-R](https://doi.org/10.1016/0016-7037(93)90414-R) (1993).
 - Kok, M. D., Rijpstra, W. I. C., Robertson, L., Volkman, J. K. & Sinninghe Damsté, J. S. Early steroid sulfurisation in surface sediments of a permanently stratified lake (Ace Lake, Antarctica). *Geochim. Cosmochim. Acta* [https://doi.org/10.1016/S0016-7037\(99\)00430-5](https://doi.org/10.1016/S0016-7037(99)00430-5) (2000).
 - Grice, K. et al. Effects of zooplankton herbivory on biomarker proxy records. *Paleoceanography* <https://doi.org/10.1029/98PA01871> (1998).
 - Witkowski, C. R., van der Meer, M. T. J., Blais, B., Sinninghe Damsté, J. S. & Schouten, S. Algal biomarkers as a proxy for pCO₂: Constraints from late Quaternary sapropels in the eastern Mediterranean. *Org. Geochem.* 104123 <https://doi.org/10.1016/j.orggeochem.2020.104123> (2020).
 - Schoell, M., Scheuten, S., Sinninghe Damsté, J. S., de Leeuw, J. W. & Summons, R. E. A molecular organic carbon isotope record of Miocene climate changes. *Science (1979)* <https://doi.org/10.1126/science.263.5150.1122> (1994).
 - Schouten, S., Schoell, M., Rijpstra, W. I. C., Sinninghe Damsté, J. S. & de Leeuw, J. W. A molecular stable carbon isotope study of organic matter in immature Miocene Monterey sediments, Pismo basin. *Geochim. Cosmochim. Acta* [https://doi.org/10.1016/S0016-7037\(97\)00062-8](https://doi.org/10.1016/S0016-7037(97)00062-8) (1997).
 - Pagani, M., Freeman, K. H. & Arthur, M. A. Isotope analyses of molecular and total organic carbon from Miocene sediments. *Geochim. Cosmochim. Acta* **64**, 37–49 (2000).
 - Witkowski, C. R., Weijers, J. W. H., Blais, B., Schouten, S. & Sinninghe Damsté, J. S. Molecular fossils from phytoplankton reveal secular pCO₂ trend over the Phanerozoic. *Sci. Adv.* **4**, eaat4556 (2018).
 - Schouten, S. et al. Biosynthetic effects on the stable carbon isotopic compositions of algal lipids: Implications for deciphering the carbon isotopic biomarker record. *Geochim. Cosmochim. Acta* [https://doi.org/10.1016/S0016-7037\(98\)00076-3](https://doi.org/10.1016/S0016-7037(98)00076-3) (1998).
 - Tipple, B. J., Meyers, S. R. & Pagani, M. Carbon isotope ratio of Cenozoic CO₂: A comparative evaluation of available geochemical proxies. *Paleoceanography* <https://doi.org/10.1029/2009pa001851> (2010).
 - Mook, W. G., Bommerson, J. C. & Staverman, W. H. Carbon isotope fractionation between dissolved bicarbonate and gaseous carbon dioxide. *Earth Planet Sci. Lett.* [https://doi.org/10.1016/0012-821X\(74\)90078-8](https://doi.org/10.1016/0012-821X(74)90078-8) (1974).
 - Kim, J.-H. et al. New indices and calibrations derived from the distribution of crenarchaeal isoprenoid tetraether lipids: Implications for past sea surface temperature reconstructions. *Geochim. Cosmochim. Acta* **74**, 4639–4654 (2010).

41. Schouten, S., Hopmans, E. C., Schefuß, E. & Sinninghe Damsté, J. S. Distributional variations in marine crenarchaeotal membrane lipids: a new tool for reconstructing ancient sea water temperatures? *Earth Planet Sci. Lett.* **204**, 265–274 (2002).
42. Bidigare, R. R. et al. Consistent fractionation of ^{13}C in nature and in the laboratory: Growth-rate effects in some haptophyte algae. *Global Biogeochem Cycles* <https://doi.org/10.1029/96GB03939> (1997).
43. Weiss, R. F. Carbon dioxide in water and seawater: the solubility of a non-ideal gas. *Mar Chem* [https://doi.org/10.1016/0304-4203\(74\)90015-2](https://doi.org/10.1016/0304-4203(74)90015-2) (1974).
44. Goericke, R., Montoya, J. P. & Fry, B. Physiology of isotopic fractionation in algae and cyanobacteria. in *Stable isotopes in ecology and environmental science* (1994).
45. Pancost, R. D., Freeman, K. H., Wakeham, S. G. & Robertson, C. Y. Controls on carbon isotope fractionation by diatoms in the Peru upwelling region. *Geochim Cosmochim Acta* [https://doi.org/10.1016/S0016-7037\(97\)00351-7](https://doi.org/10.1016/S0016-7037(97)00351-7) (1997).
46. Sinninghe Damsté, J. S., Kuypers, M. M. M., Pancost, R. D. & Schouten, S. The carbon isotopic response of algae, (cyano) bacteria, archaea and higher plants to the late Cenomanian perturbation of the global carbon cycle: Insights from biomarkers in black shales from the Cape Verde Basin (DSDP Site 367). *Org. Geochem* **39**, 1703–1718 (2008).
47. Bice, K. L. et al. A multiple proxy and model study of Cretaceous upper ocean temperatures and atmospheric CO_2 concentrations. *Paleoceanography* <https://doi.org/10.1029/2005PA001203> (2006).
48. Naafs, B. D. A. et al. Gradual and sustained carbon dioxide release during Aptian Oceanic Anoxic Event 1a. *Nat. Geosci.* <https://doi.org/10.1038/ngeo2627> (2016).
49. Kamikuri, S. & Motoyama, I. Variation in the eastern North Pacific subtropical gyre (California Current system) during the Middle to Late Miocene as inferred from radiolarian assemblages. *Mar. Micropaleontol.* **155**, 101817 (2020).
50. Palmer, M. R. et al. Multi-proxy reconstruction of surface water $p\text{CO}_2$ in the northern Arabian Sea since 29ka. *Earth Planet Sci. Lett.* <https://doi.org/10.1016/j.epsl.2010.03.023> (2010).
51. Sosdian, S. M. et al. Constraining the evolution of Neogene ocean carbonate chemistry using the boron isotope pH proxy. *Earth Planet Sci. Lett.* **498**, 362–376 (2018).
52. Steinthorsdottir, M., Jardine, P. E. & Rember, W. C. Near-future $p\text{CO}_2$ during the hot miocene climatic optimum. *Paleoceanogr. Paleoclimatol* **36**, e2020PA003900 (2021).
53. Goldner, A., Herold, N. & Huber, M. The challenge of simulating the warmth of the mid-Miocene climatic optimum in CESM1. *Clim. Past* <https://doi.org/10.5194/cp-10-523-2014> (2014).
54. Krapp, M. & Jungclauss, J. H. The Middle Miocene climate as modelled in an atmosphere-ocean-biosphere model. *Clim. Past* <https://doi.org/10.5194/cp-7-1169-2011> (2011).
55. Knorr, G., Butzin, M., Micheels, A. & Lohmann, G. A warm Miocene climate at low atmospheric CO_2 levels. *Geophys. Res. Lett.* <https://doi.org/10.1029/2011GL048873> (2011).
56. Westerhold, T. et al. An astronomically dated record of Earth's climate and its predictability over the last 66 million years. *Science* (1979) **369**, 1383–1387 (2020).
57. Martínez-Botí, M. A. et al. Plio-Pleistocene climate sensitivity evaluated using high-resolution CO_2 records. *Nature* <https://doi.org/10.1038/nature14145> (2015).
58. Royer, D. L. Climate sensitivity in the geologic past. *Annu. Rev. Earth Planet Sci.* **44**, 277–293 (2016).
59. Kiehl, J. T. & Shields, C. A. Sensitivity of the Palaeocene-Eocene Thermal Maximum climate to cloud properties. *Philos. Trans. R. Soc. A: Math. Phys. Eng. Sci.* <https://doi.org/10.1098/rsta.2013.0093> (2013).
60. Sagoo, N., Valdes, P., Flecker, R. & Gregoire, L. J. The early Eocene equable climate problem: Can perturbations of climate model parameters identify possible solutions? *Philos. Trans. R. Soc. A: Math. Phys. Eng. Sci.* <https://doi.org/10.1098/rsta.2013.0123> (2013).
61. Zhu, J. & Poulsen, C. J. Quantifying the cloud particle-size feedback in an earth system model. *Geophys. Res. Lett.* <https://doi.org/10.1029/2019GL083829> (2019).
62. Lunt, D. J. et al. A model-data comparison for a multi-model ensemble of early Eocene atmosphere-ocean simulations: EoMIP. *Clim. Past* <https://doi.org/10.5194/cp-8-1717-2012> (2012).
63. Scotese, C. An estimate of the volume of Phanerozoic ice. *Earth Space Sci. Open Arch.* <https://doi.org/10.1002/essoar.10500763.1> (2020).
64. Baatsen, M. et al. The middle-to-late Eocene greenhouse climate, modelled using the CESM 1.0.5. *Clim. Past Dis.* <https://doi.org/10.5194/cp-2020-29> (2020).
65. Rohling, E. J., Medina-Elizalde, M., Shepherd, J. G., Siddall, M. & Stanford, J. D. Sea surface and high-latitude temperature sensitivity to radiative forcing of climate over several glacial cycles. *J. Clim.* <https://doi.org/10.1175/2011JCLI4078.1> (2012).
66. Forster, P. M., Maycock, A. C., McKenna, C. M. & Smith, C. J. Latest climate models confirm need for urgent mitigation. *Nat. Clim. Chang* **10**, 7–10 (2020).
67. Hopcroft, P. O. et al. Polar amplification of Pliocene climate by elevated trace gas radiative forcing. *Proc. Natl. Acad. Sci.* **117**, 23401–23407 (2020).
68. Katz, B. J. & Elrod, L. W. Organic geochemistry of DSDP Site 467, offshore California, Middle Miocene to Lower Pliocene strata. *Geochim. Cosmochim. Acta* [https://doi.org/10.1016/0016-7037\(83\)90261-2](https://doi.org/10.1016/0016-7037(83)90261-2) (1983).
69. Sinninghe Damsté, J. S. & de Leeuw, J. W. Analysis, structure and geochemical significance of organically-bound sulphur in the geosphere: State of the art and future research. *Org. Geochem.* [https://doi.org/10.1016/0146-6380\(90\)90145-P](https://doi.org/10.1016/0146-6380(90)90145-P) (1990).
70. Sinninghe Damsté, J. S., Irene, W., Rijpstra, C., de Leeuw, J. W. & Schenck, P. A. Origin of organic sulphur compounds and sulphur-containing high molecular weight substances in sediments and immature crude oils. *Org. Geochem.* [https://doi.org/10.1016/0146-6380\(88\)90079-4](https://doi.org/10.1016/0146-6380(88)90079-4) (1988).
71. Schouten, S. et al. An interlaboratory study of TEX86 and BIT analysis using high-performance liquid chromatography–mass spectrometry. *Geochem. Geophys. Geosyst.* **10**, <https://doi.org/10.1029/2008GC002221> (2009).
72. Schouten, S., Hugué, C., Hopmans, E. C., Kienhuis, M. V. M. & Sinninghe Damsté, J. S. Analytical methodology for TEX86 paleothermometry by high-performance liquid chromatography/atmospheric pressure chemical ionization-mass spectrometry. *Anal. Chem.* **79**, 2940–2944 (2007).
73. Hopmans, E. C., Schouten, S. & Sinninghe Damsté, J. S. The effect of improved chromatography on GDGT-based palaeoproxies. *Org. Geochem* **93**, 1–6 (2016).
74. Dowsett, H. et al. The PRISM4 (mid-Piacenzian) paleoenvironmental reconstruction. *Clim. Past* <https://doi.org/10.5194/cp-12-1519-2016> (2016).

Acknowledgements

We thank Vittoria Lauretano for researching updates to the age model, Jort Ossebaar, Alle Tjipke Hoekstra, and Ronald van Bommel at the NIOZ for technical support, and Jack Middelburg, Heather Stoll, and Roderik van der Wal for scientific input. This study received funding from the Netherlands Earth System Science Centre (NESSC) through a gravitation grant (024.002.001) to JSSD and SS from the Dutch Ministry for Education, Culture and Science. AvdH and PJV acknowledge support from the TiPES project ('Tipping Points in the Earth System') from the European Union's Horizon 2020 research and innovation programme under

grant agreement no. 820970. CRW is supported by the Royal Society Dorothy Hodgkin Fellowship (DHF\R1\221014).

Author contributions

C.R.W., S.S. and J.S.S.D. designed the study and wrote the manuscript. C.R.W. and MvdM analysed samples. ASvdH and P.J.V. conducted climate sensitivity analysis. All authors interpreted the data and contributed to the manuscript.

Competing interests

The authors declare no competing interests.

Additional information

Supplementary information The online version contains supplementary material available at <https://doi.org/10.1038/s41467-024-47676-9>.

Correspondence and requests for materials should be addressed to Caitlyn R. Witkowski.

Peer review information *Nature Communications* thanks the anonymous reviewer(s) for their contribution to the peer review of this work. A peer review file is available.

Reprints and permissions information is available at <http://www.nature.com/reprints>

Publisher's note Springer Nature remains neutral with regard to jurisdictional claims in published maps and institutional affiliations.

Open Access This article is licensed under a Creative Commons Attribution 4.0 International License, which permits use, sharing, adaptation, distribution and reproduction in any medium or format, as long as you give appropriate credit to the original author(s) and the source, provide a link to the Creative Commons licence, and indicate if changes were made. The images or other third party material in this article are included in the article's Creative Commons licence, unless indicated otherwise in a credit line to the material. If material is not included in the article's Creative Commons licence and your intended use is not permitted by statutory regulation or exceeds the permitted use, you will need to obtain permission directly from the copyright holder. To view a copy of this licence, visit <http://creativecommons.org/licenses/by/4.0/>.

© The Author(s) 2024